Journal of Solid State Chemistry 182 (2009) 2961–2971

Contents lists available at ScienceDirect

Journal of Solid State Chemistry

journal homepage: www.elsevier.com/locate/jssc

Spin-state transition of iron in $(Ba_{0.5}Sr_{0.5})(Fe_{0.8}Zn_{0.2})O_{3-\delta}$ perovskite

Armin Feldhoff [a,*], Julia Martynczuk [a,1], Mirko Arnold [a], Maxym Myndyk [b], Ingo Bergmann [b,2], Vladimir Šepelák [b,3,4], Wolfgang Gruner [c], Ulrich Vogt [d], Angelika Hähnel [e], Jörg Woltersdorf [e]

[a] Institut für Physikalische Chemie und Elektrochemie, Leibniz Universität Hannover, D-30167 Hannover, Germany
[b] Institut für Physikalische und Theoretische Chemie, Technische Universität Braunschweig, D-38104 Braunschweig, Germany
[c] Leibniz-Institut für Festkörper- und Werkstoffforschung Dresden, D-01069 Dresden, Germany
[d] EMPA, Materials Science & Technology, CH-8600 Dübendorf, Switzerland
[e] Max-Planck-Institut für Mikrostrukturphysik, D-06120 Halle, Germany

ARTICLE INFO

Article history:
Received 4 May 2009
Received in revised form
10 July 2009
Accepted 18 July 2009
Available online 6 August 2009

Keywords:
Perovskite
Valence
Spin-state
Mössbauer spectroscopy
EELS

ABSTRACT

The redox behavior of iron during heating of a high-performance perovskite for ceramic oxygen separation membranes was studied by combined electron energy-loss (EELS, esp. ELNES) and Mössbauer spectroscopical *in situ* methods. At room temperature, the iron in $(Ba_{0.5}Sr_{0.5})(Fe_{0.8}Zn_{0.2})O_{3-\delta}$ (BSFZ) is in a mixed valence state of 75% Fe^{4+} in the high-spin state and 25% Fe^{3+} predominantly in the low-spin state. When heated to 900 °C, a slight reduction of iron is observed that increases the quantity of Fe^{3+} species. However, the dominant occurrence is a gradual transition in the spin-state of trivalent iron from a mixed low-spin/high-spin to a pure high-spin configuration. In addition, a remarkable amount of hybridization is found in the Fe–O bonds that are highly polar rather than purely ionic. The coupled valence/spin-state transition correlates with anomalies in thermogravimetry and thermal expansion behavior observed by X-ray diffraction and dilatometry, respectively. Since the effective cationic radii depend not only on the valence but also on the spin-state, both have to be considered when estimating under which conditions a cubic perovskite will tolerate specific cations. It is concluded that an excellent phase stability of perovskite-based membrane materials demands a tailoring, which enables pure high-spin states under operational conditions, even if mixed valence states are present. The low spin-state transition temperature of BSFZ provides that all iron species are in a pure high-spin configuration already above ca. 500 °C making this ceramic highly attractive for intermediate temperature applications (500–800 °C).

1. Introduction

Ceramic membranes can provide remarkable oxygen permeation fluxes at infinite selectivity without the need of external electrodes when they are based on heavily doped anion deficient cubic perovskite-type $A_{1-x}A'_xB_{1-y}B'_yO_{3-\delta}$ oxides exhibiting mixed oxygen-ion and electron conductivities at elevated temperatures (500–1000 °C) [1]. While the partial conductivity of electrons is distinctly higher than that of oxygen ions [1,2], the oxygen deficit δ correlates directly with the obtainable permeation flux via the concentration of disordered oxygen vacancies. The perovskite lattice can tolerate a remarkable number of vacant oxygen sites if a reducible transition metal cation is located at the crystallographic *B* site in the center of the BO_6 octahedron. Upon heating under constant pressure, entropy may free up even more oxygen from a previously equilibrated perovskite. The quantity of released oxygen may be quite high as the requirement of charge neutrality is no longer preserved solely by small concentrations of cation vacancies but by the possibly flexible redox behavior of the *B* site cation(s). However, one requirement for the oxygen vacancies to be mobile is to preserve a cubic perovskite structure [3], where the redox behavior of the *B* site cation(s) plays the key role as well. Hence, a better understanding of the redox behavior can be used to tailor improved membrane materials with excellent phase stability under strongly reducing conditions.

The pioneering work of Teraoka et al. in the 1980s [4–7] exceeded the already high standards for obtainable oxygen fluxes. As a consequence, the search for high-flux materials (i.e., exhibiting oxygen permeation fluxes of one to two orders of magnitude higher than cubically stabilized zirconia equipped

* Corresponding author.
E-mail address: armin.feldhoff@pci.uni-hannover.de (A. Feldhoff).
[1] Now at: Nonmetallic Inorganic Materials, ETH Zurich, Wolfgang-Pauli-Str. 10, CH-8093 Zurich, Switzerland.
[2] Now at: Suzuki Laboratory, Institute of Multidisciplinary Research for Advanced Materials, Tohoku University, Sendai 980-8577, Japan.
[3] On leave from the Institute of Geotechnics, Slovak Academy of Sciences, SK-04353 Košice, Slovak Republic.
[4] Now at: Institute of Nanotechnology, Karlsruhe Institute of Technology, Hermann-von-Helmholtz-Platz 1, D-76344 Eggenstein-Leopoldshafen, Germany.

0022-4596/$ - see front matter © 2009 Elsevier Inc. All rights reserved.
doi:10.1016/j.jssc.2009.07.058

with shortcircuit external electrodes [4,8]) focused until today mostly on complex perovskites hosting cobalt on their crystallographic *B* site. The current state-of-the-art material with respect to oxygen permeation and phase stability above 900 °C is $(Ba_{0.5}Sr_{0.5})(Co_{0.8}Fe_{0.2})O_{3-\delta}$ (BSCF) [3,9–11]. Recently, *in situ* high-temperature electron energy-loss spectroscopy (HT-EELS) on BSCF has shown that cobalt is reduced from an average formal oxidation state of 2.6+ to 2.2+ and iron from 3.0+ to 2.8+, if BSCF is heated in the vacuum chamber of a transmission electron microscope (TEM) from room temperature to 950 °C [12]. The average valence of the *B* site cations, 2.7+ at room temperature and 2.3+ at 950 °C, give oxygen contents $3-\delta$ of 2.3 and 2.2, respectively. That is in good agreement with oxygen stoichiometries estimated by thermogravimetric analysis (TGA) and neutron powder diffraction [13]. The experiments in [12] however, give direct proof of the easier reducibility of cobalt over iron in a highly doped perovskite-type oxide. Also, comparative TGA of different perovskite-type materials indicate that during heating the polyvalent *B*-site cobalt ions are reduced far more easily than iron, manganese or nickel [14].

The flexible redox behavior of cobalt provides on the one hand high oxygen fluxes at high temperatures. On the other hand it leads to two major problems hindering the reliable use of the BSCF material (and cobaltites in general) under important technical requirements. First, it causes a large coefficient of thermal expansion (CTE) that can lie in the range of $20-24\times10^{6}\,K^{-1}$ over a wide temperature range [13,15]. The resulting dilatation causes huge thermal stresses and thus cracks form easily in the membranes, especially if operated at steep oxygen potential gradients. Steep gradients can be obtained by making membranes very thin (i.e., $<200\,\mu m$) [15–17]. This is of interest to increase flux densities for the design of compact membrane units. Second, the valence instability of cobalt introduces inherent phase instability to the cobaltites at intermediate temperatures (ITs, ca. 500–800 °C) [9,18,19]. This is due to a coupled valence/spin-state transition of cobalt, and cobaltites containing CoO_6 octahedra with Co^{3+} in low-spin configuration tend to prefer face sharing (contributions of hexagonal stacking) rather than corner sharing (cubic stacking) [19]. The breakdown of the cubic perovskite structure principally limits the long-time stability of the BSCF material under the conditions required for the operation of a membrane material in the IT range. The IT range, however, is of special interest for membrane-based dehydrogenation processes in the synthesis of basic chemicals like ethylene [20] and propylene [21] at high selectivity, and for the novel concept of solid oxide fuel cells (SOFCs) [22].

Recently, the search for alternative materials has led to the development of the cobalt-free perovskite-type oxide $(Ba_{0.5}Sr_{0.5})(Fe_{0.8}Zn_{0.2})O_{3-\delta}$ (BSFZ) [23,24]. Wang et al. [24] demonstrated its potential for use in a membrane reactor for the partial oxidation of methane (POM) at 900 °C. The reported oxygen permeation flux of $2.5\,ml\,min^{-1}\,cm^{-2}$ on 1.25 mm-thick membranes at 900 °C indicates a high conductivity as well as high surface exchange rates for oxygen. Wei et al. [25,26] quantified the latter by measuring low polarization resistances of 0.22, 0.46, and $0.98\,\Omega\,cm^2$ at 700, 650, and 600 °C, respectively. They also used BSFZ as a cathode material in an IT-SOFC at 500–650 °C at power densities up to $180\,mW\,cm^{-2}$. The room temperature structure of BSFZ has been refined in a cubic unit cell ($a=0.3990(0)\,nm$) by the Rietveld method [27]. *In situ* X-ray diffraction (XRD) has shown that BSFZ remains in the cubic structure if heated to 900 °C in air or in low oxygen partial pressures down to 10×10^{-7} Pa [24]. Good phase stability of cubic BSFZ in the IT range has been demonstrated recently for up to 100 h [28] and it is further implied by the observation that the perovskite can be synthesized by a sol–gel-based method in the pure phase at 750 °C [27,29,30]. This is contrary to the cobaltite BSCF that requires higher temperatures in an analogous synthesis (950 °C) [19,31]. The present work focuses on a thorough atomic level understanding of electronic effects in the redox behavior of the BSFZ perovskite. Combined *in situ* electron energy-loss spectroscopy (EELS) and Mössbauer spectroscopy show that a coupled Fe^{4+}/Fe^{3+} valence and Fe^{3+} low-spin to high-spin transition play a key role. This is reflected in anomalies found in integrative investigations of temperature-dependent weight-losses and lattice dilatations.

2. Material and methods

The BSFZ material was synthesized from nitrate precursors via an ethylene-diamine-tetra-acetic acid (EDTA)/citrate acid complexing method at 950 °C for 10 h as described in detail elsewhere [27,29,30]. BSFZ ceramics were sintered at 1150 °C for 10 h and shaped by cutting, grinding, and polishing into disks approximately 3 mm in diameter and 80 μm in thickness. To obtain TEM specimens, these disks were dimple grinded from one side to a residual thickness of 10 μm (dimple grinder, model 656, Gatan Inc., Pleasanton, CA, USA). Finally, Ar^+ ion sputtering was employed at 3 kV under an incident angle of 6° (PIPS, precision ion polishing system, model 691, Gatan Inc.,) until electron transparency was achieved.

To obtain a standard for Fe^0, a metallic iron wire 0.25 mm in diameter (purity 99.99 + %, Chempur) was polished on polymer-embedded diamond foils to a thickness of 50 μm using 1,2-propanediol as a lubricant. The bar was epoxy-glued onto a copper slot grid (1×2 mm; 50 μm) and then ion-milled with 3 kV–Ar^+. The specimen was immediately transferred from the vacuum chamber of the ion mill to the transmission electron microscope (TEM). To prevent the undesired influence of local oxidation of thin specimen areas on the observed EEL fine structures near the $L_{2,3}$ ionization edge of iron (Fe $L_{2,3}$-ELNES), it was carefully checked for the absence of any O-K signal in EEL and energy dispersive X-ray (EDX) spectra. Commercial powders of $FeTiO_3$ (purity 99.8%, Alfa Aesar, CAS-No. 12022-71-8) and $\alpha-Fe_2O_3$ (>95%, Riedel-de-Haen, CAS-No. 1309-37-1) were used as standards for Fe^{2+} and Fe^{3+}, respectively. $FeTiO_3$ (ilmenite) is a more reliable standard for Fe^{2+} than FeO (wüstite), as the latter is often iron deficient and consists of $Fe_{1-x}O$ with noticeable contributions of Fe^{3+} [32]. To obtain a standard for Fe^{4+}, a procedure similar to those chosen in [33,34] was applied; although here an EDTA/citrate acid complexing method (like for the synthesis of the BSFZ material) instead of a solid-state process was used to synthesize $SrFeO_{3-\delta}$. Phase purity was confirmed by XRD. Subsequently, stoichiometric $SrFeO_3$ was observed by filling the lattice with additional oxygen. The additional oxygen was inserted into the lattice using $KClO_4$ in a gold capsule with an internal oxygen pressure of approximately 9 bar (six-fold excess) in an autoclave under 1.2 kbar and 530 °C for 22 h. All standards were carefully checked by Mössbauer spectroscopy to exhibit just the desired iron valence. For TEM, the powders were crushed, dispersed in ethanol, dropped onto copper-supported holey carbon films, and dried.

TEM investigations at room temperature (JEM-2100F-UHR, $C_S=0.5$ mm, $C_C=1.2$ mm, JEOL Ltd., Tokyo, Japan) and at high temperature (CM20 FEG Super TWIN microscope, $C_S=1.2$ mm, $C_C=1.2$ mm, Philips, Eindhoven, Netherlands) were performed at 200 kV with the specimen at $2–4\times10^{-5}$ Pa. Both microscopes were equipped with a post-column imaging filter (GIF, Gatan Inc.) employing a 1024×1024 pixel charge-coupled device (CCD) camera and a light-element EDX spectrometer. The Schottky-type emitter gave a full width at half maximum (FWHM) of the zero-loss peak of 1 eV. Calibration of the GIF drift tubes was done using

the first maximum of the Ni–L_3 edge of an NiO standard (853 eV [35]). The energy dispersion of the spectrometer setup at nominally 0.1 eV/pixel was calibrated by acquiring the zero-loss peak with an offset of 50 eV given to the calibrated drift tube and without any offset. All EEL spectra were taken in diffraction-coupled mode. Magnifications of the TEMs were set in combination with a 2 mm entrance aperture of the GIF so that ca. 150 nm circular areas were analyzed. These were carefully chosen to be thin and in the case of powder specimens were not supported locally by a carbon film. An objective aperture was inserted to limit the collection half-angle to ca. 32 mrad, respectively. This means that the dipole selection rule primarily applies and restricts, with respect to parity and angular momentum, the nature of empty states to be probed. In principle this provides measurement of the site, spin-state, and symmetry of the selected ions. To measure the absolute position of core-loss details, pairs of core-loss and low-loss spectra were acquired with 10 s exposure, while the switching of energy ranges was made within a few seconds by removing offsets to the drift tube of the GIF (O-K: 530 eV; Fe–$L_{2,3}$: 710 eV; Ba–$M_{4,5}$: 780 eV). Illumination was almost parallel but was adjusted for low-loss acquisition by defocusing the condensor lens (CL-3) to avoid overexposure of the CCD camera. The CM20FEG was equipped with a double tilting heating holder (model 652-Ta, Gatan Inc.). Heating from room temperature to 900 °C was done with a ramp of ca. 5 °C min^{-1}, and the specimen was equilibrated at the respective temperature for 15 min before acquiring *in situ* EEL spectra.

Scanning electron microscopy (SEM) was made on a field-emission instrument at 2 kV (JSM-6700F, JEOL Ltd., Tokyo, Japan).

Mössbauer spectroscopic measurements were performed in transmission geometry using a conventional spectrometer in constant acceleration mode. *In situ* spectra were taken in the temperature range of 20–900 °C in air. BSFZ powder specimen was fixed on a quartz support (a 200 μm thick plate). A ^{57}Co/Rh γ-ray source was used. The velocity scale of the spectra was calibrated relative to ^{57}Fe in Rh. "Recoil" spectral analysis software [36] was used for the quantitative evaluation of the Mössbauer spectra. The Voigt-based fitting method provided distributions of hyperfine parameters for multiple species in a spectrum.

Differential thermoanalysis (DTA) and TGA were measured on 99.5 mg calcined BSFZ powder in a DTA/TG crucible of Al_2O_3 from 20–1400 °C with a heating rate of 5 °C/min under an air flowrate of 100 ml min^{-1} (STA 429 CD, Netsch, Selb, Germany). The oxygen content of calcined BSFZ powder was measured by the carrier gas hot extraction method with a commercial oxygen analyzer (TC 436DR, Leco, St. Joseph, USA). The powders were weighed (about 20 mg) into a metallic capsule of nickel (0.4 g) with the addition of a tin tablet (0.2 g). This pressed package was dropped into an outgassed high temperature graphite crucible that was electrically heated with a power–time-program. Two infrared selective detectors registered simultaneously the formed reaction species CO and CO_2. The calibration was carried out with ZrO_2 for the CO detector and with carbon dioxide gas dosing for the CO_2 detector. A reproducibility of 0.5% relative standard deviation (RSD) for this method has been shown for many oxides [37].

In situ high-temperature XRD measurements were performed with monochromator-filtered Cu$K\alpha$ radiation ($K\alpha_2/K\alpha_1$: 0.5) at 40 kV and 40 mA with a receiving slit of 0.19 mm (X'pert-MPD instrument, Philips). Data were collected in a step-scan mode in the range of 29–33° 2Θ with intervals of 0.02° and count times of 30 s per step. The sample was tested in an HT cell (HDK 2.4 with REP 2000, Edmund Bühler, Hechingen, Germany) with a Pt–Rh holder, which has no reflection in the applied 2Θ range. The applied temperature range was 30–1000 °C with 3 °C min^{-1} in air and an equilibrium time of 30 min for each data acquisition. The maximum of the (110) reflection was estimated by a combined Gaussian and Lorentzian fitting, and the cell parameters were refined by using TOPAS-Academic V4.1 (Coelho Software, Brisbane, Australia).

Measurements of the linear thermal expansion of BSFZ ceramics were conducted in the 20–1000 °C range, using a difference dilatometer with inductive transducers (DIL 802L, Bähr, Hüllhorst, Germany). Quartz specimens were used for calibration and as inert bodies. To study the influence of p_{O_2}, the expansion measurements were carried out in a flowing gas atmosphere of argon (0.5 Pa O_2) and argon/O_2 mixtures under different O_2 partial pressures. In all cases, dense rods ($5 \times 2 \times 15$ mm^3) with polished frontal faces were successively heated and cooled two times at the rate 5 °C min^{-1}. The coefficient of thermal expansion (CTE) follows directly from these measurements as for the cubic perovskite the strain tensor is fully determined by a single scalar [38].

3. Results and discussion

Fig. 1 illustrates the sol–gel-based synthetic process for BSFZ starting from an aqueous solution of stoichiometric amounts of nitrates with EDTA, citric acid, and ammonia. The stage of the gel (after 18 h at 150 °C) is characterized by an ultrafine dispersion of cross-linked metal–organic complexes (bright features in Fig. 1a). The fine-scale intermixing is considered a major advantage over classical solid-state routes if a homogeneous product of complex stoichiometry is desired, as in case of BSFZ. After calcination, the BSFZ perovskite is a fine powder with grains of nanoscale size that are eventually sintered together (Fig. 1b). After green compacting and sintering at ambient pressure, a BSFZ ceramic is obtained with grain sizes in the order of several tens of micrometers (Fig. 1c).

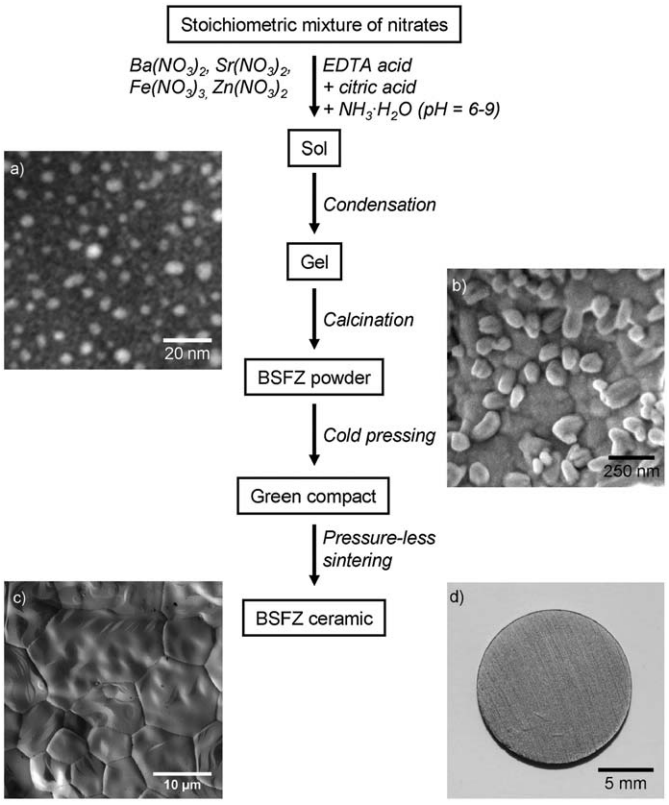

Fig. 1. From nano to macro. Outline of the sol–gel-based synthetic process with snapshots of different steps: (a) STEM-HAADF of the gel showing finely dispersed and cross-linked metal–organic complexes, (b) SEM of calcined perovskite powder, (c) SEM surface view of grain structure in sintered BSFZ ceramic, (d) photograph of a disk membrane.

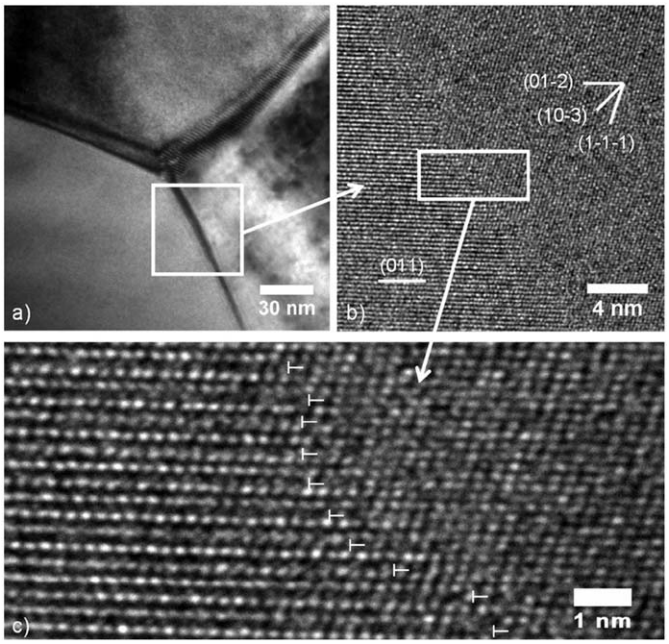

Fig. 2. Details of a grain boundary in a BSFZ ceramic: (a) TEM bright-field of a triple junction, (b) HRTEM with indices assigned to lattice planes, (c) HRTEM with indication of unpaired atomic planes.

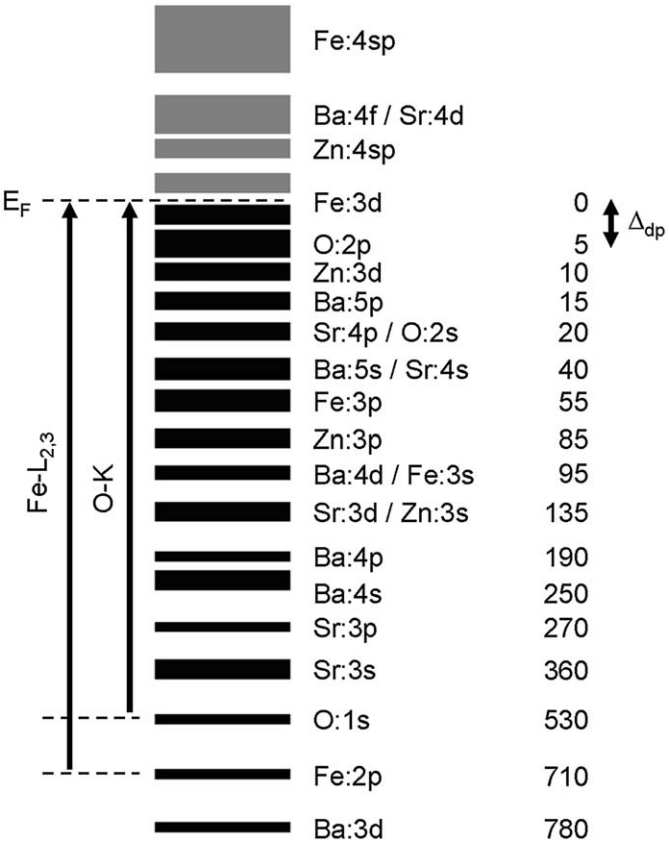

Fig. 3. Schematic sketch of the electronic states or energy bands in the cubic BSFZ perovskite with binding energies down to 780 eV. Electronic transitions from O:1s and Fe:2*p* into unoccupied states above the Fermi level E_F indicate the origin of O K and Fe $L_{2,3}$-ELNES.

Ceramic membranes for oxygen permeation experiments are disks having 14 mm diameter and 1.2 mm thickness (Fig. 1d) or fibers having a diameter of 1 mm and a wall thickness of 150 μm [39].

The grain boundaries in sintered membranes are atomically thin, with the absence of any interfacial phase. A typical example is shown in Fig. 2. The lattice misfit between the (011) lattice planes of grain A (0.282 nm) and the $(01\bar{2})$ lattice planes of grain *B* (0.178 nm) is accommodated by misfit dislocations (marked by *T*'s in Fig. 2c). Obviously, it is energetically favorable to reduce strain by leaving every third $(01\bar{2})$ atomic plane of grain *B* unpaired, and thus loose coherency. In [40,41] it was shown that this kind of grain boundary acts as a barrier for oxygen permeation. In the present article, however, we focus on the bulk properties of the BSFZ material during temperature-induced reduction.

It is therefore essential to have a look at the electronic states or bands in the BSFZ material (Fig. 3). The location of the O:2*p* states just a few eV below the partly filled Fe:3*d* states means a small electronic oxygen ligand to iron charge transfer energy $\Delta_{dp} = \varepsilon_{Fe:3d} - \varepsilon_{O:2p}$ [42]. This causes partial hybridization in the Fe–O bonds that become strongly polar rather than purely ionic. For the same reason, hybridization of O:2*p* with unoccupied Zn:4*sp*, Ba:4*f*, Sr:4*d*, and Fe:4*sp* is expected (see Fig. 3). Because the occupied O:2*p* and Zn:3*d* states are energetically similar, an anomalous valence band cation:*d*–anion:*p* hybridization is expected as well [43].

Starting with an ionic model for iron allows important details of the electronic structure to be derived. The average *d* electron energy is given by the electrostatic Madelung energy of the ions. Due to intra-atomic exchange coupling, indistinguishable electrons in the partly filled 10 *d* orbitals cause a splitting by Δ_{ex} [44]. This splits the *d* states for majority spin "+" and minority spin "−" (Fig. 4). It has to be taken into account that iron is octahedrally coordinated by oxygen in the cubic perovskite structure. Thus, the additional crystal field splitting Δ_c of the two sets of five *d* orbitals into three t_{2g} and two e_g orbitals, respectively, has to be considered. Depending on the relative magnitude of Δ_{ex} and Δ_c there are different electronic configurations, three of which are shown in Fig. 4: high-spin Fe^{IV} with $3d^4_{HS} = (t^+_{2g})^3(e^+_g)^1$, low-spin Fe^{iii} with $3d^5_{LS} = (t^+_{2g})^3(t^-_{2g})^2$, and high-spin Fe^{III} with $3d^5_{HS} = (t^+_{2g})^3(e^+_g)^2$. Consider that the amount of hybridization is different for the three configurations. The e_g orbitals are directed to the ligand, giving a large overlap with O:2*p* orbitals. The t_{2g} orbitals point towards the corners of the cubic unit cell and overlap less with the O:2*p* orbitals. It can be assumed that the amount of hybridization of e_g is twice that of t_{2g} [45] due to a stronger overlap with O:2*p* orbitals. As a consequence e_g-derived bands are broader than t_{2g}-derived bands, even though both bands are narrow.

Fig. 5 shows the room temperature $L_{2,3}$ energy-loss near-edge structures (ELNESs) of iron in different compounds exhibiting pure valence states [46] compared to the BSFZ material (gray curves).

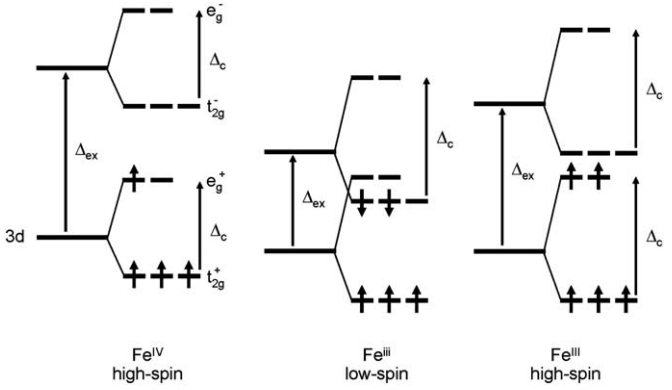

Fig. 4. Electronic configurations for iron ions in an octahedral ligand field.

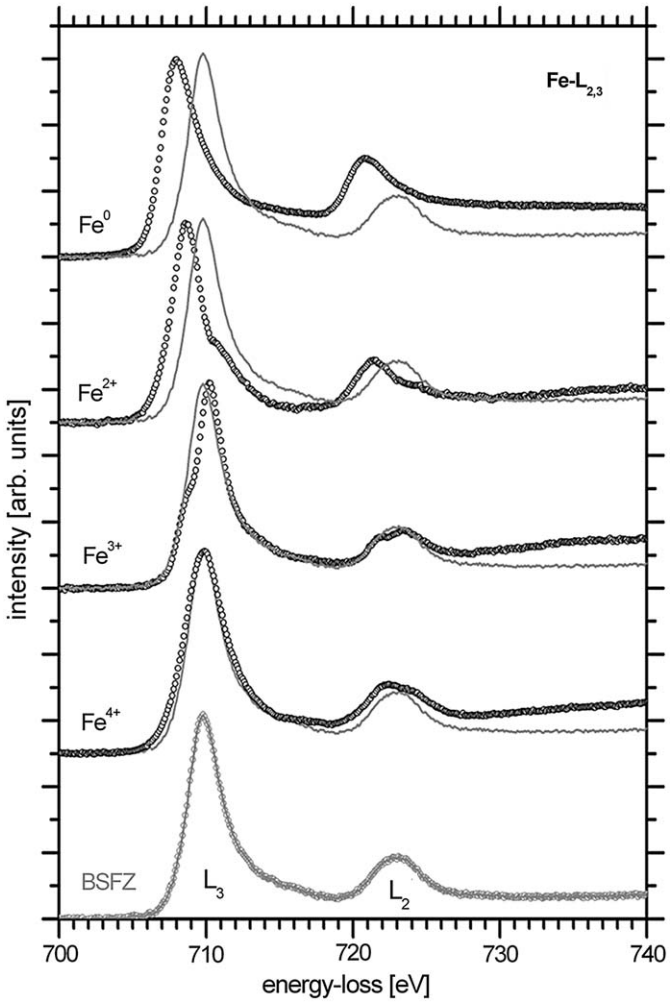

Fig. 5. Room temperature ELNES of iron $L_{2,3}$ for different ionization states: Fe^0 (metallic iron), Fe^{2+} ($FeTiO_3$), Fe^{3+} (α–Fe_2O_3), and Fe^{4+} ($SrFeO_3$). Gray curves refer to a BSFZ ceramic. Spectra are background subtracted, scaled to the same height of the respective maximum, and vertically shifted for clarity.

Because of Fe:2*p* spin–orbit coupling, the overall spectral shapes are similar for all iron species with an intense peak at around 708–710 eV (L_3) and a less intense peak at 721–723 eV (L_2). Respective spectra in Fig. 5 match those obtained for FeO (Fe^{2+}), $LaFeO_3$ (Fe^{3+}), and $SrFeO_3$ (Fe^{4+}) by X-ray absorption near-edge structures (XANES) and by multi-electron configuration interaction calculations [47,48]. These findings show that the chemical shift between Fe^0, Fe^{2+}, Fe^{3+}, and Fe^{4+} is in the range of 2 eV, making accurate measurement of the absolute position of fine structure details essential. Positions of the first peak (L_3) in the Fe $L_{2,3}$-ELNES in Fig. 5 were estimated by the weighted centroid's abscissa, based on the non-linear least squares fitting of multiple Gaussian functions (see [12]), respectively. The first peak in the Fe^0 $L_{2,3}$-ELNES has its centroid's abscissa at 708.1 eV, and the whole spectrum is in agreement with the one presented in [49]. The centroid's abscissa of the L_3 peak of $FeTiO_3$ (Fe^{2+}) is located at 709.3 eV and that of α–Fe_2O_3 (Fe^{3+}) at 710.8 eV. The high-energy shoulders of the L_3 and L_2 peaks of Fe^{2+} as well as the low-energy shoulders of the L_3 and L_2 peaks of Fe^{3+} are usually taken as indications of a high-spin state of iron in the crystal field of the oxygen ligand, respectively [50,51]. The L_3 peak of $SrFeO_3$ (Fe^{4+}) has its centroid's abscissa at 710.7 eV. The centroid's abscissa of the first peak in the Fe $L_{2,3}$-ELNES of the BSFZ material is at 710.6 eV and coincides with that of the Fe^{3+} and Fe^{4+} standards. The L_2 peak centroid's abscissa is at 723.0 eV. The overall shape and position of the $L_{2,3}$-ELNES suggests an Fe^{4+}/Fe^{3+} mixed valence of iron in the BSFZ material at room temperature. It is noted that other spectral regions of the BSFZ material are shown in [30]. Because the L_3 and L_2 peaks in all the oxides presented do not split significantly it is concluded that the crystal field splitting Δ_c and the intra-atomic exchange splitting Δ_{ex} having nearly identical values (cf. Fig. 4). However, the first peak in the $L_{2,3}$-ELNES of the Fe^{2+} and Fe^{3+} standards still shows some splitting. In contrast, this peak does not show any separation for the Fe^{4+} standard or BSFZ, and the full width at half maximum is just 3.5 eV and 2.8 eV, respectively. Hence, the energy difference $|\Delta_{ex} - \Delta_c|$ in BSFZ is even smaller than for all investigated oxide standards. Moreover, it is concluded that the absolute values of Δ_{ex} and Δ_c are small compared to the actual energy resolution of 1 eV in the experiments. That means that the e_g^+ and t_{2g}^- states are positioned almost at the same energy leading to the competition of high- and low-spin states and the eventual break down of Hund's rule [44].

The ELNES of Fe–$L_{2,3}$ and O-K edges of the BSFZ material were monitored from room temperature to 900 °C. Significant changes in shape or energy position were not observed. Some *in situ* spectra of Fe–$L_{2,3}$ are shown in Fig. 6. Over the entire temperature range they show similar features to those discussed for the BSFZ

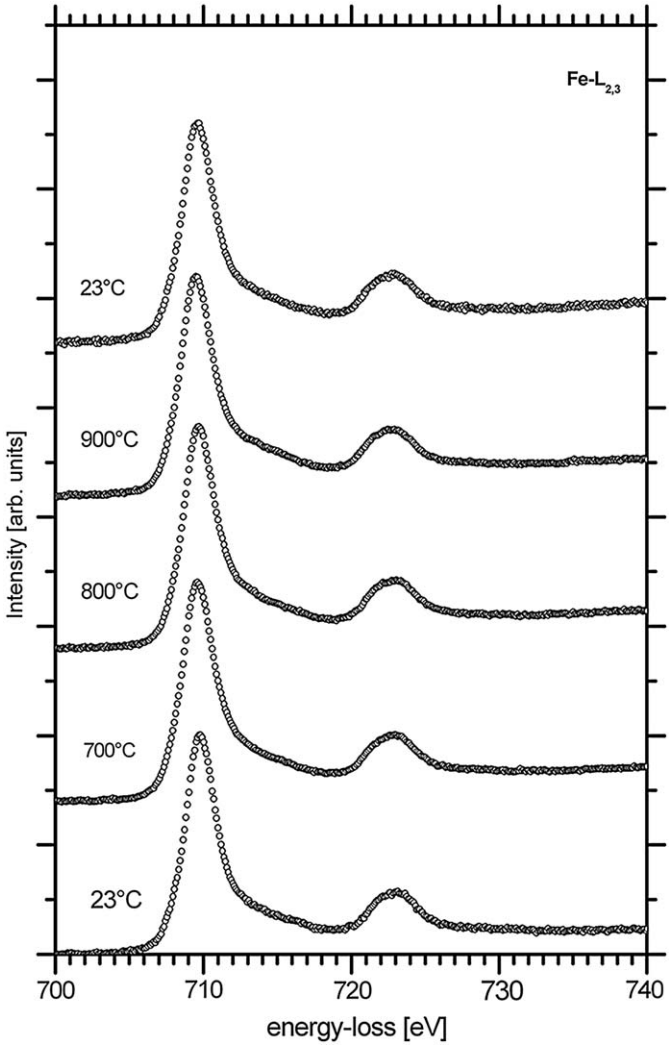

Fig. 6. *In situ* iron $L_{2,3}$-ELNES of a BSFZ ceramic. Spectra are background subtracted, scaled to the same height of the first maximum, and vertically shifted for clarity.

spectrum in Fig. 5 with the same peak width and separations, indicating that iron stays in an Fe^{4+}/Fe^{3+} mixed valence state during the *in situ* experiment.

The O K-ELNES of the *in situ* spectra (Fig. 7) can be divided into three regions: pre-peak A, peak B, and peak C. Pre-peak A (522–530.5 eV) originates from transitions of O:1*s* electrons into the unoccupied Fe:3*d* fraction that have 2*p* character due to hybridization with O:2*p* orbitals [12,45,52,53]. If compared with [43,54,55], peak B (530.5–546 eV) can be assigned to Zn:4*sp*, Ba:4*f*, and Sr:4*d* orbitals hybridized with O:2*p* orbitals (see Fig. 3). Feature C (above 546 eV) are unoccupied Fe:4*s* and Fe:4*p* states weakly hybridized with O:2*p* orbitals (see Fig. 3). Neither fitting procedures [12,52] or integration of intensities gave a trend in the relative amount of pre-peak A as a function of temperature. Integration revealed that the relative amount of the pre-peak A intensities in the spectral range from 522–546 eV scatters from 13% to 15%. It is concluded that the amount of O:2*p* hybridization with Fe:3*d* relative to that with other metal cations does not change with the bond length expansion associated with lattice dilatation during heating of BSFZ. However, a shoulder in the high-energy flank of peak B is noted at high temperatures, and it remains present after cooling of the specimen to room temperature. It must be noted that if the heating occurs in the vacuum chamber of a TEM, the reverse filling oxygen in the perovskite lattice will not reach the initial level. A more accurate designation of the spectral features in the high-energy flank of peak B would require band structure calculations for this complex perovskite that is beyond the scope of this work. Nevertheless, because the pre-peak A does not show splitting, it is emphasized once again that the energies Δ_{ex} and Δ_c as well as their difference $|\Delta_{ex} - \Delta_c|$ are small in BSFZ under all experimental conditions.

Room temperature Mössbauer spectra of a BSFZ powder before and after heat treatments in air up to 900 °C are almost identical (see Fig. 8). However, a small difference is noted that hints to some irreversibility in the oxygen release and pick-up process. The room temperature spectra are well fitted by the superposition of three subspectra (Fig. 8, bottom). Based on their isomer shifts ($IS_{black} = -0.19$ mm/s, $IS_{light\ gray} = 0.26$ mm/s) and on their symmetric quadrupole splitting ($QS_{black} = 0.48$ mm/s, $QS_{light\ gray} = 1.11$ mm/s) these black and light gray subspectra are attributed to Fe^{IV}, $(t_{2g}^{+})^3(e_g^{+})^1$, and Fe^{III} ions, $(t_{2g}^{+})^3(e_g^{+})^2$, respectively, both in octahedral coordination and high-spin configurations [56–58]. The isomer shift of the third subspectrum ($IS_{dark\ gray} = 0.53$ mm/s) can be attributed to Fe^{iii}, $(t_{2g}^{+})^3(t_{2g}^{-})^2$, also in octahedral coordination [56,58–61], but in a low-spin configuration. It should be noted that the dark gray subspectrum shows almost no quadrupole splitting and supports the above made designation of *d* orbital occupancies that give different electric field gradients at the iron nucleus [58]. The average relative intensities of the subspectra, calculated from the room temperature spectrum before the heating cycle, are as follows: $I_{black} = 67.9\%, I_{dark\ gray} = 24.0\%, I_{light\ gray} = 8.1\%$. In Fig. 8 it is shown that the dark gray subspectrum disappears with increasing temperature from room temperature to ca. 500 °C.

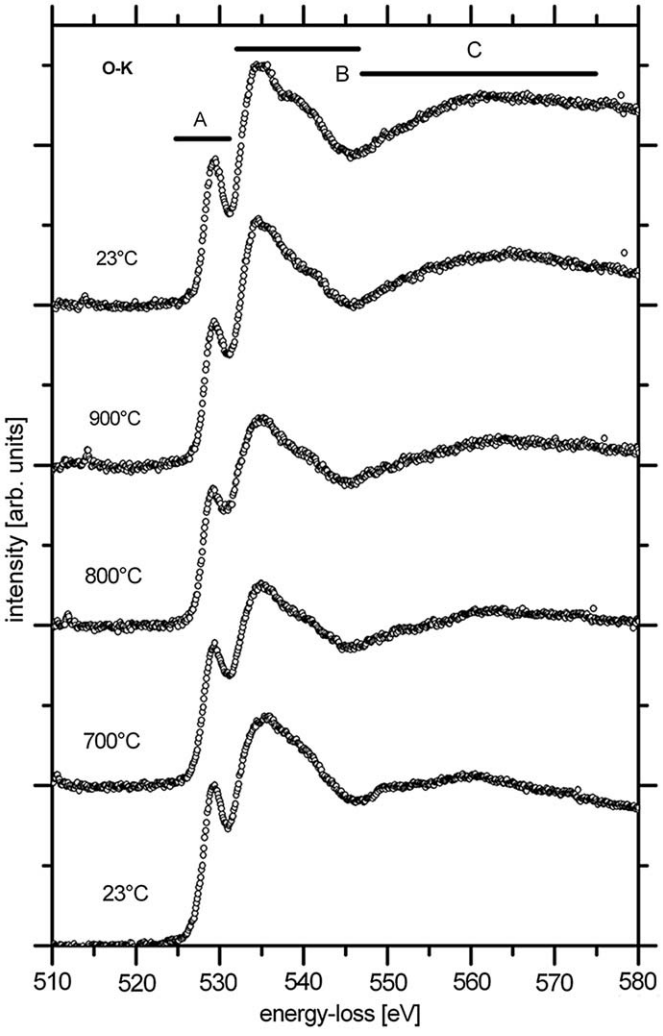

Fig. 7. *In situ* oxygen K-ELNES of a BSFZ ceramic. Spectra are background subtracted, scaled to the same integral counts in the range of 522–546 eV, and vertically shifted for clarity.

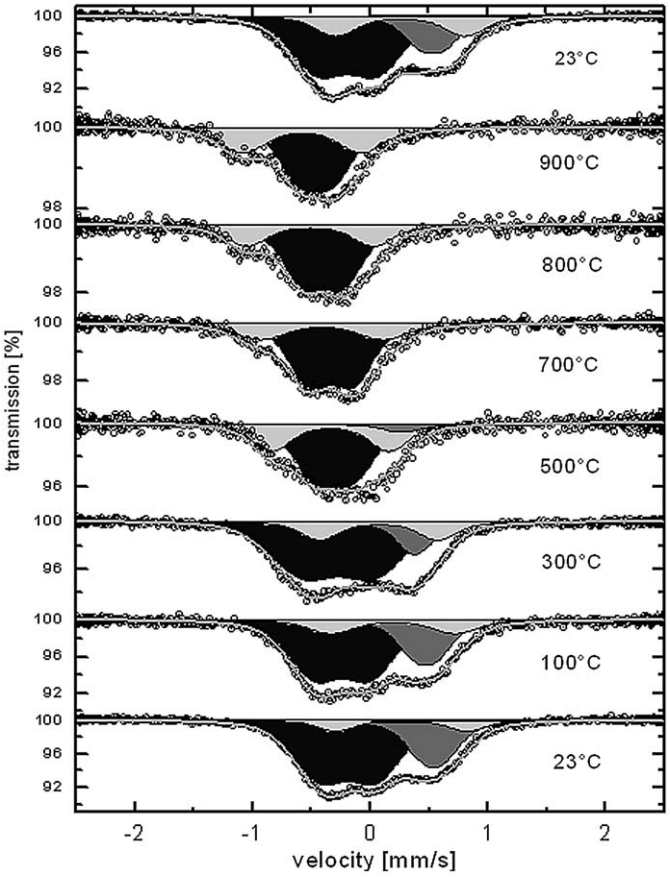

Fig. 8. *In situ* Mössbauer spectra of BSFZ powder conducted in air. The subspectra are fitted in color (Fe^{IV} black, Fe^{iii} dark gray, and Fe^{III} light gray) and are vertically shifted for clarity.

At temperatures above 500 °C, the spectra become narrower. The vanishing of the Fe^{iii} fraction from the spectrum indicates a partial spin-state transition by an increase of $\Delta_{ex} - \Delta_c$ (cf. Fig. 4). The Mössbauer spectra of the sample taken above 500 °C could be fitted by the superposition of just two subspectra (black and light gray). The intensity of the light gray subspectrum increases at the expense of the black one. At 900 °C, the intensities of the light gray and black subspectra are 37.5% Fe^{III} and 62.5% Fe^{IV}, respectively (see Table 1 for more details).

If the intensities of the subspectra are taken to indicate the relative amount of different iron species, a very slight reduction of iron is noted; the deduced oxygen stoichiometry $3-\delta$ of the BSFZ compound does not change significantly, from 2.67 at room temperature to 2.65 at 900 °C in air. The change in iron valencies deduced would be minimal, 3.7+ at room temperature and 3.6+ at 900 °C, respectively. But the mixed low- and high-spin state of the Fe^{3+} ion changes to a purely high-spin configuration. For room temperature the deduced δ (and corresponding iron valences) are in good agreement with Fig. 9, but, at high temperature they deviate remarkably by an underestimation of Fe^{3+} species. Remember, the spectral intensities of subspectra are proportional to the recoil-free fraction of various iron species in the sample and can be correlated directly to real concentrations only if constant atomic displacement factors are assumed for all species. Even though in the cubic perovskite the different iron species occupy just one crystallographic site, a measure of likely individual thermal vibration amplitudes has to be estimated by temperature-dependent neutron, X-ray or (convergent beam) electron diffraction on single-crystals combined with appropriate modeling. This is of special concern for the BSFZ perovskite, as the average atomic displacement parameter for the 1*b* Wyckoff position (iron and zinc) is already high as $B = 2.4 \pm 0.1$ at room temperature [29]. The situation is even more complicated by the complex stoichiometry of BSFZ. However, to allow a reliable quantification of the spectra once additional knowledge about the BSFZ material is obtained, we provide complete spectral information in a condensed form in Table 1.

In addition, it should be mentioned that with increasing temperature there is a large center shift of all subspectra to the left. This means essentially that the charge density at the ^{57}Fe nucleus decreases [58] even though a contribution from second-order Doppler shift [62,63] should be considered. One principal reason for the observation could be a decrease of the probability density of ligand orbitals (oxygen) at the position of the ^{57}Fe nucleus when the lattice is thermally dilated. The second principal reason is related to the observed spin-state transition and a change in the population of orbitals with e_g- and t_{2g}-character. Remember, the amount of hybridization of e_g orbitals pointing to the ligand, can be assumed to be twice that of t_{2g} orbitals due to larger overlap integrals with O:2*p* orbitals [45,44].

Table 1
Fitting results of the *in situ* Mössbauer spectra of BSFZ.[a]

T (°C)	Fe^{IV} high-spin			Fe^{iii} low-spin			Fe^{III} high-spin			CS (mm s^{-1})
	IS (mm s^{-1})	QS (mm s^{-1})	Intensity (%)	IS (mm s^{-1})	QS (mm s^{-1})	Intensity (%)	IS (mm s^{-1})	QS (mm s^{-1})	Intensity %	
23	−0.19	0.48	67.9	+0.53	0.21	24.0	+0.26	1.11	8.1	+0.02
100	−0.23	0.50	62.0	+0.47	0.21	24.0	+0.20	1.06	14.0	0.00
300	−0.27	0.64	69.5	+0.38	0.14	14.0	+0.08	1.00	16.5%	−0.12
500	−0.30	0.33	62.5	+0.27	0.18	4.8	−0.34	1.00	32.7	−0.29
700	−0.33	0.39	74.3	–	–	–	−0.41	1.05	25.7	−0.35
800	−0.40	0.36	71.8	–	–	–	−0.51	1.08	28.2	−0.43
900	−0.46	0.30	62.5	–	–	–	−0.57	1.00	37.5	−0.50
23	−0.19	0.51	61.7	+0.53	0.21	19.7	+0.26	1.10	18.6	+0.04

[a] A Lorentzian linewidth of 0.24 mm s^{-1} resulting from the fit of the room temperature spectrum of the sample was chosen for the fits of the spectra taken at elevated temperatures. CS refers to the center shift of the whole spectrum.

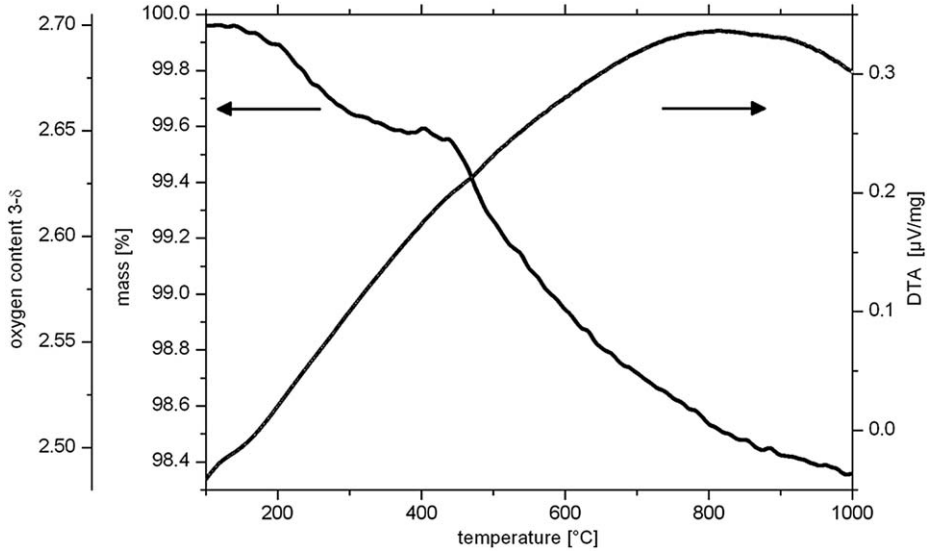

Fig. 9. DTA and TGA curves of BSFZ with indication of the oxygen content $3-\delta$.

DTA probes the thermal stability of the perovskite by the absence of exo- or endothermic peaks in the temperature range from 100 to 1000 °C (see Fig. 9, right scale). Hence, crystallographic phase transformations or abrupt decomposition can be ruled out. The constant increase of the DTA signal displays an exothermic process spanning from 100 to 900 °C and is attributed to the release of oxygen from the perovskite lattice. The oxygen release is monitored by a continuous weight loss as seen in the TGA curve (Fig. 9, left scale). The slope of the TGA curve becomes distinctly steeper at around 450 °C, correlating with the vanishing of the Fe^{iii} fraction (cf. Fig. 8). It should be noted that the resulting high-spin configurations have a higher occupancy of the e_g-based states (see Fig. 4) with stronger hybridization effects and thus a higher electronegativity. This is favorable for a larger release rate of oxygen. The accompanied reduction of iron is obviously easier if no spin-flip are involved. However, above 800 °C the mass loss (Fig. 9, left scale) becomes very small and the oxygen release seams to stagnate at a relative weight loss of ca. 1.6 wt%. The DTA shows constant values above 800 °C and decreases above 900 °C, signifying the end of the exothermic process, i.e., the oxygen release. The oxygen content in a BSFZ powder at room temperature was estimated by carrier hot gas extraction to 20.25 ± 0.19 wt% after double heating–cooling in a thermoanalyzer apparatus (STA449, Netzsch, Selb, Germany) between room temperature and 1000 °C at a heating/cooling rate of 20 °C min^{-1}. The measurements gave an oxygen content $3-\delta$ of about 2.70 ± 0.03. Using this data, the TGA curve can be interpreted directly in terms of the oxygen content in the BSFZ perovskite (Fig. 9, very left scale). It shows a decrease of the oxygen content from 2.70 at room temperature to 2.50 at 900 °C. That corresponds to a reduction of iron from an average valence of 3.75+ down to 3.25+, if the other cations are considered to have a constant valence: Ba^{2+}, Sr^{2+}, and Zn^{2+}. In other words, iron in BSFZ is in a mixed 75% Fe^{4+}/25% Fe^{3+} valence at room temperature. Upon heating to 900 °C in air it will be reduced to a 25% Fe^{4+}/75% Fe^{3+} valence. We should mention that the TGA curve in Fig. 9 agrees with the one published by Wei et al. [26] for the heating of BSFZ in air. However, their room temperature value for the oxygen content estimated by iodiometric titration is lower (2.59). Thus, they estimate the oxygen content at 900 °C to be just 2.40, which would implicitly predict a reduction of iron to less than 3+ with some Fe^{2+} species being present. However, this can be ruled out by Mössbauer spectroscopy (Fig. 8) as well as by EELS (Figs. 5 and 6). We state that our results are self-consistent.

In situ XRD patterns of a BSFZ powder in air and in reducing gas mixtures (Ar, 2% O_2–Ar, and 2% H_2–Ar) in the 2θ range of 20°–90° from room temperature to 900 °C have been presented in [24]. They show excellent phase stability under all applied conditions by the conservation of the cubic perovskite structure. Fig. 10 shows the 2θ angular position of the (110) reflection of the cubic BSFZ during *in situ* heating in air up to 1000 °C with indication of the respective lattice parameters. The absolute peak position after the heating cycle is shifted by 0.1° towards larger angles and indicates that the changes are not completely reversible, probably due to kinetic effects. This is consistent with observations by EELS (cf. Fig. 7) and Mössbauer spectroscopy (cf. Fig. 8). A change in the rate of expansion of the BSFZ powder crystals is noted between 400 and 600 °C. From these XRD data, the CTE is estimated to be around 11×10^{-6} and 24×10^{-6} K^{-1} in the temperature ranges 30–400 °C and 600–1000 °C, respectively.

The dilatometric measurement of the CTE for a BSFZ ceramic is presented in Fig. 11 as a function of different oxygen partial pressure. The measurements were conducted at 100% and 20% O_2, and under Ar. The CTE is nearly independent of the oxygen partial pressure p_{O_2}, although it slightly decreases with decreasing p_{O_2}. There is a constant CTE between 300–600 °C of ca. 15×10^{-6} K^{-1}

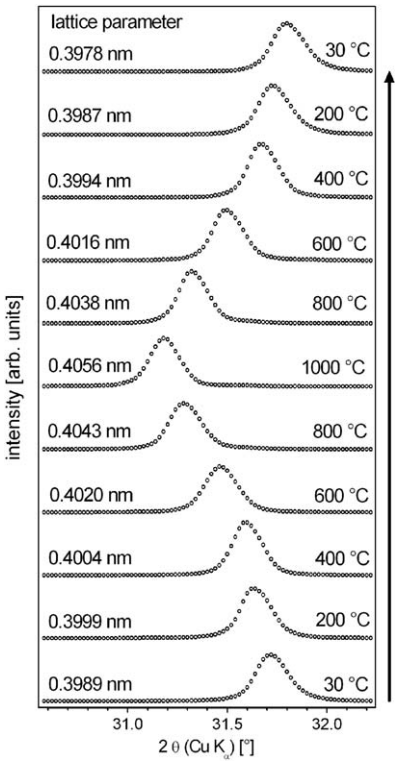

Fig. 10. *In situ* XRD pattern in air of a narrow angular range around the (110) reflection of a BSFZ powder with indication of respective lattice parameters for the cubic cell. Diffractograms are vertically shifted for clarity.

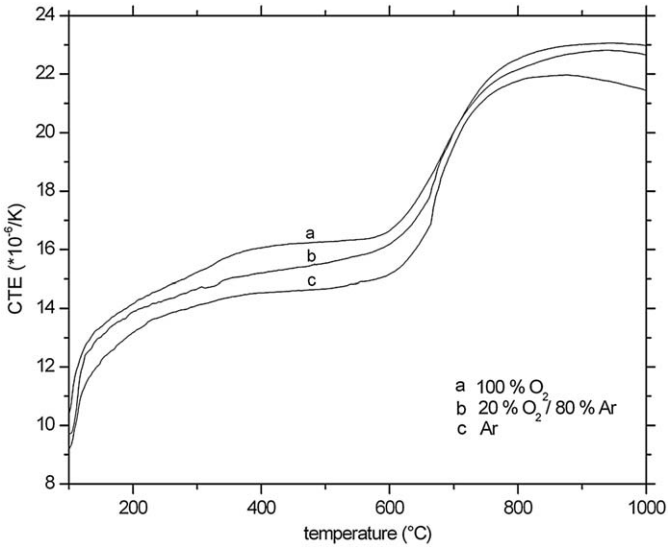

Fig. 11. Coefficient of thermal expansion of BSFZ as a function of temperature for different oxygen partial pressures: (a) 100% O_2, $p_{O_2} \approx 100$ kPa, (b) 20% O_2, $p_{O_2} \approx 20$ kPa, (c) "pure" argon, <3 ppm O_2, $p_{O_2} \leq 0.3$ Pa.

and between 750 and 1000 °C of ca. 22×10^{-6} K^{-1}, which corresponds to the XRD data obtained on powders. Strain-induced phase transitions can be ruled out by the *in situ* XRD and DTA observations. Therefore, the CTE in the current experiment is a combination of a steady thermal expansion caused by anharmonic thermal lattice vibrations and an additional term of a chemical expansion [64,65] due to the coupled valence/spin-state transition of iron and the accompanied increase of its ionic radius during heating.

4. Conclusions

The performed EELS, esp. ELNES analyses of the Fe−$L_{2,3}$ edge have revealed that iron in the BSFZ perovskite is in a mixed Fe^{4+}/Fe^{3+} valence state at room temperature. Upon heating to 900 °C the reduction of iron is so weak that no Fe^{2+} species are involved. Moreover, at the O-K edge hybridization effects of O:2*p* orbitals with empty Fe:3*d*, Zn:4*sp*, Ba:4*f*, Sr:4*d*, and Fe:4*sp* orbitals are noticed. The relative amount of hybridization does not change upon heating of the BSFZ perovskite. Mössbauer spectroscopy identified a gradual spin-state transition of the Fe^{3+} species from a mixed low-spin/high-spin configuration to a high-spin configuration. Above ca. 500 °C the Fe^{3+} fraction is in a pure high-spin state. The Fe^{4+} fraction is in a pure high-spin state under all applied conditions. Concerning the redox state of iron, weights of Mössbauer subspectra give a reliable estimate at room temperature only. At elevated temperatures obviously the Fe^{3+} recoil-free fraction is lower than the Fe^{4+} recoil-free fraction as a consequence of different temperature coefficients of the respective atomic displacement parameters. However, the accurate determination of the oxygen content by carrier hot gas extraction ($3-\delta=2.70$) gave an average Fe valence of 3.75+ in BSFZ at room temperature. Based on these values, monitoring the released amount of oxygen by weight loss upon heating shows that the oxygen content drops to 2.50 and iron is reduced to an average valence of 3.25+ at 900 °C in air. The oxygen release rate and the accompanied reduction of iron increase at around 450 °C, which is the Fe^{3+} spin-state transition. The spin-state transition also reflects in an increase of lattice expansion above ca. 600 °C as monitored by XRD and dilatometry. Consider that unusual thermal expansion has been reported also in the spin-state transition of $LaCoO_3$ [66]. Note that for BSFZ the quadrupole splitting of Fe^{4+} and the isomer shifts show discontinuities at the spin-state transition (see Table 1). Similar observations have been made in case of a pressure-induced spin-state transition of $LaFeO_3$ [67].

The spin-state transition should be elucidated in more detail. Since the intra-atomic exchange coupling Δ_{ex} decreases with larger radial extension of the crystalline wave functions [44], $\Delta_{ex}(Fe^{4+})$ exceeds $\Delta_{ex}(Fe^{3+})$. Increasing Δ_{ex} with decreasing hybridization is forced by a lattice expansion in our experiments. Contrary, the cubic ligand field splitting Δ_c increases with increasing hybridization and $\Delta_c(Fe^{4+})<\Delta_c(Fe^{3+})$. An increase of the Fe–O distance, and thus smaller Fe:3*d*–O:2*p* interactions leads to a lower Δ_c and a more stable high-spin state. As oxygen is located at the face centers of the cubic unit cell, the Fe–O distance can be read for different temperatures directly from Fig. 10 as half of the respective lattice parameter. It increases from 199.5 pm at room temperature, to 200.0 pm at 400 °C, to 201.0 pm at 600 °C, and so forth. The effective ionic radii from Shannon's compilation [68] for Fe^{IV} (58.5 pm), Fe^{III} (64.5 pm), and Fe^{iii} (55.0 pm) sum with that of O^{2-} (140.0 pm) to 198.5 pm, 204.5 pm, and 195.0 pm, respectively. The lack of additivity to the bond length of the radii of the Fe^{3+} species can be attributed to some covalence (covalent shortening) and maybe electron delocalization [68]. It directly points at the higher electronegativity of Fe^{3+} compared to Fe^{4+} in the perovskite framework. The corresponding Fe:3*d*–O:2*p* hybridization is indeed proved by the pre-peak A in the O K-ELNES (Fig. 7). However, the consideration of summarized effective ionic radii indicates that it is favorable for iron to leave the low-spin configuration with increasing Fe–O bond length. Changes in the occupancy of t_{2g} and e_g states affect the amount of hybridization and the strength of Fe–O bonds, so additional anharmonic terms are introduced into the elastic energy. This might be the reason why the spin-state transition correlates with the observed changes in the rate of lattice expansion (cf. Figs. 10 and 11). The decrease of hybridization with thermal expansion is reflected in the center shift of the Mössbauer spectra (cf. Fig. 8 and Table 1). Remember that the elastic energy is anharmonic in principle. Otherwise, no thermal expansion would be observed and the amplitude of atomic vibrations would rise without a shift of the center of gravity with increasing temperature [38].

The redox chemistry of transition metals in these complex perovskites cannot be described by a simple change in valence. Hybridization enables gradual charge transfer in bonds with oxygen and thus changes of the electronegativity of the transition metal during oxidation or reduction [69]. From the transition metals perspective lattice expansion corresponds to an oxidation and removal of oxygen from the lattice to a reduction. For the heating of BSFZ, reduction of iron from Fe^{4+} to Fe^{3+} is compensated partly by the O:2*p* band. Lowering p_{O_2} in the surrounding atmosphere, i.e., picking more oxygen from the perovskite lattice, gives two electrons per removed oxygen atom to the lattice and may enhance hybridization of Fe:3*d*–O:2*p* bonds. The Fe–O bonds become stronger with decreasing p_{O_2} and we expect a smaller CTE. This systematic trend can be seen in Fig. 11.

We restricted our discussion of the electronic structure in context with Fig. 3 somehow to a simple ionic model with electrons being localized around iron sites to highlight some important points. However, the excellent transport properties of BSFZ for oxygen ions and electrons [24–26] suggest further investigations of the t_{2g}- and e_g-based energy bands are warranted. The e_g orbitals with higher amount of hybridization give broader bands. The partly filled t_{2g}^{+}- and e_g^{-}-based bands are narrow and not widely separated, which is essential in the observed spin-state transition and indicated by the sharp first peak (2.8 eV FWHM) in the Fe $L_{2,3}$-ELNES (Figs. 5 and 6). The spin-state transition is manifested in the crossing and finally the separation of t_{2g}^{+}- and e_g^{-}-based bands. A maximum in the electrical conductivity of BSFZ at around 600 °C (9.4 S cm^{-1}), observed by Wei et al. [26], manifests a transition from thermally activated polaronic electron hopping to metallic conduction, which was pointed out by some authors to be equivalent with a spin-state transition [70,71]. Comparison with structural field maps [72–74] indeed shows that BSFZ is located close to the borderline of localized to itinerant behavior of the iron *d* electrons, which can be crossed by changes in stoichiometry or external parameters, and unusual properties can be expected.

Oxygen K-ELNES showed that the amount of O:2*p* hybridization with Fe:3*d* relative to other metal cations (Zn:4*sp*, Ba:4*f*, and Sr:4*d*) does not change with the bond length expansion associated with lattice dilatation during heating of BSFZ. This is in clear contrast to observations in the BSCF perovskite, which show a relative switch in hybridization of O:2*p* with Ba:4*f* and Sr:4*d* upon Fe:3*d* and Co:3*d* [12]. The comparison with [43] makes the relative stabilization of transition-metal–oxygen-ligand to earth alkaline-metal–oxygen-ligand hybridization plausible by an anomalous Zn:3*d*–O:2*p* hybridization caused by a very small energy difference (cf. Fig. 3).

It is worth noting that the lowest temperature of successful synthesis of BSCF (950 °C) [19,31] or BSFZ (750 °C) [27,29,30] correlates with spin-state transitions of one of the polyvalent transition metal ions. As already mentioned, it has to be emphasized that both, valence and spin-state, modify the effective radii of transition metal cations, which govern Goldschmidt's tolerance factor, providing a principal criterion for the expectable perovskite symmetry. Therefore, a careful choice of a membrane material for specific operational conditions has to take into account, that a high stability of the cubic perovskite structure can only be achieved in a pure high-spin state material with its higher ionic radius. This is seen as a big advantage for BSFZ in the IT

range compared to BSCF. However, spin-state transition and its effect on the functionality of membrane materials must be investigated in more detail.

Integration over the CTE from room temperature to 700 °C (Fig. 11) gives a dilatation of 0.94% for BSFZ, compared to 1.6% for the cobaltite BSCF (based on the CTE given in [13]). The relatively low dilatation of the BSFZ material combined with the peculiar redox behavior of iron, good transport properties, and phase stability [24–26] makes it superior to cobaltites for prospective applications in the intermediate temperature range (500−800 °C).

5. Summary

It has been shown that the iron in the BSFZ perovskite has a mixed 75% Fe^{4+}/25% Fe^{3+} valence (3.75+) at room temperature. Upon heating to 900 °C in air it is reduced to a 25% Fe^{4+}/75% Fe^{3+} valence (3.25+). The Fe^{4+} fraction is always in a high-spin state, and the Fe^{3+} fraction makes a transition from a predominantly low-spin to a pure high-spin configuration at intermediate temperatures. A decrease in the amount of Fe:3*d*–O:2*p* hybridization during lattice expansion is seen as the reason for the spin-state transition as the exchange coupling Δ_{ex} increases and the cubic ligand-field splitting Δ_c decreases for each species. The coupled valence/spin-state transition is seen as anomalies of weight-loss, due to release of oxygen, and thermal expansion behavior. It is concluded that to provide excellent phase stability of perovskite-based membrane materials it is crucial to tailor the materials in a way that they exhibit pure high-spin states under operational conditions, even in the presence of mixed valence states. This is the case for BSFZ above ca. 500 °C, making it highly attractive for intermediate temperature applications (500−800 °C).

Acknowledgments

We would like to thank Prof. Harald Behrens for putting his high-pressure apparatus at our disposal and Dr. Falk Heinroth for assistance in TGA measurements. Our discussions with Profs. Jürgen Caro and Haihui Wang were fruitful and are appreciated. This work was financially supported by the Deutsche Forschungsgemeinschaft (DFG) under Grant FE 928/1-2. V.Ŝ. thanks the DFG for supporting his work in the framework of the Priority Program *"Crystalline Nonequilibrium Phases"* (SPP 1415). Partial support by the Alexander von Humboldt Foundation, the APVV (0728-07), and the VEGA (2/0065/08) is gratefully acknowledged.

References

[1] J. Sunarso, S. Baumann, J. Serra, W. Meulenberg, S. Liu, Y. Lin, J.D. da Costa, Mixed ionic–electronic conducting (MIEC) ceramic-based membranes, J. Membr. Sci. 320 (2008) 13–41.
[2] H. Bouwmeester, Dense ceramic membranes for methane conversion, Catal. Today 82 (2003) 141–150.
[3] J. Vente, S. McIntosh, W. Haije, H. Bouwmeester, Properties and performance of $Ba_xSr_{1-x}Co_{0.8}Fe_{0.2}O_{3-\delta}$ materials for oxygen transport membranes, J. Solid State Electrochem. 10 (2006) 581–588.
[4] Y. Teraoka, H. Zhang, S. Furukawa, N. Yamazoe, Oxygen permeation through perovskite-type oxides, Chem. Lett. (1985) 1743–1746.
[5] H. Zhang, Y. Teraoka, N. Yamazoe, Mixed ionic–electronic conductivity of $La_{1-x}Sr_xCo_{1-y}Fe_yO_{3-\delta}$ perovskite-type oxides, Chem. Lett. (1987) 665–668.
[6] Y. Teraoka, T. Nobunaga, N. Yamazoe, Effect of cation substitution on the oxygen semipermeability of perovskite-type oxides, Chem. Lett. (1988) 503–506.
[7] Y. Teraoka, H. Zhang, K. Okamoto, N. Yamazoe, Mixed ionic–electronic conductivity of $La_{1-x}Sr_xCo_{1-y}Fe_yO_{3-\delta}$ perovskite-type oxides, Mater. Res. Bull. 23 (1988) 51–58.
[8] W. Kingery, J. Pappis, M. Dotty, D. Hill, Oxygen ion mobility in cubic $Zr_{0.85}Ca_{0.15}O_{1.85}$, J. Am. Ceram. Soc. 42 (1959) 393–398.
[9] Z. Shao, W. Yang, Y. Cong, H. Dong, J. Tong, G. Xiong, Investigation of the permeation behaviour and stability of a $Ba_{0.5}Sr_{0.5}Co_{0.8}Fe_{0.2}O_{3-\delta}$ oxygen membrane, J. Membr. Sci. 172 (2000) 177–188.
[10] Z. Shao, S. Haile, A high-performance cathode for the next generation of solid-oxide fuel cells, Nature 431 (2004) 170–173.
[11] S. McIntosh, J. Vente, W. Haije, D. Blank, H. Bouwmeester, Phase stability and oxygen non-stoichiometry of $SrCo_{0.8}Fe_{0.2}O_{3-\delta}$, Solid State Ionics 177 (2006) 833–842.
[12] M. Arnold, Q. Xu, F. Tichelaar, A. Feldhoff, Local charge disproportion in a high-performance perovskite, Chem. Mater. 21 (2008) 635–640.
[13] S. McIntosh, J. Vente, W. Haije, D. Blank, H. Bouwmeester, Oxygen stoichiometry and chemical expansion of $(Ba_{0.5}Sr_{0.5})(Co_{0.8}Fe_{0.2})O_{3-\delta}$ measured by in situ neutron diffraction, Chem. Mater. 18 (2006) 2187–2193.
[14] Y. Teraoka, H. Shimokawa, C. Kang, H. Kusaba, K. Sasaki, Fe-based perovskite-type oxides as excellent oxygen-permeable and reduction-tolerant materials, Solid State Ionics 177 (2006) 2245–2248.
[15] J. Vente, W. Haije, Z. Rak, Performance of functional perovskite membranes for oxygen production, J. Membr. Sci. 276 (2006) 178–184.
[16] Y. Teraoka, T. Fukuda, N. Miura, N. Yamazoe, Development of oxygen semipermeable-membrane using mixed conductive perovskite-type oxides. 2. Preparation of dense film of perovskite-type oxide on porous substrate, J. Ceram. Soc. Jpn. 97 (1989) 533–538.
[17] T. Schiestel, M. Kilgus, S. Peter, K. Caspary, H. Wang, J. Caro, Hollow fibre perovskite membranes for oxygen separation, J. Membr. Sci. 258 (2005) 1–4.
[18] S. Švarcová, K. Wiik, J. Tolchard, H. Bouwmeester, T. Grande, Structural instability of cubic perovskite $Ba_xSr_{1-x}Co_{1-y}Fe_yO_{3-\delta}$, Solid State Ionics 178 (2008) 1787–1791.
[19] M. Arnold, T. Gesing, J. Martynczuk, A. Feldhoff, Correlation of the formation and the decomposition process of the BSCF perovskite at intermediate temperature, Chem. Mater. 20 (2008) 5858–5881.
[20] H. Wang, Y. Cong, W. Yang, High selectivity of oxidative dehydrogenation of ethane to ethylene in an oxygen permeable membrane reactor, Chem. Commun. (2002) 1468–1469.
[21] H. Wang, Y. Cong, X. Zhu, W. Yang, Oxidative dehydrogenation of propane in a dense tubular membrane reactor, React. Kinet. Catal. Lett. 79 (2003) 351–356.
[22] C. Steele, A. Heinzel, Materials for fuel-cell technologies, Nature 414 (2001) 345–352.
[23] J. Caro, H. Wang, C. Tablet, G. Grubert, Sauerstofftransportierende Oxidkeramiken, EU Patent EP 1 630 148 A3, 2006.
[24] H. Wang, C. Tablet, A. Feldhoff, J. Caro, A cobalt-free oxygen-permeable membrane based on the perovskite-type oxide $(Ba_{0.5}Sr_{0.5})(Fe_{0.8}Zn_{0.2})O_{3-\delta}$, Adv. Mater. 17 (2005) 1785–1788.
[25] B. Wei, Z. Lü, X. Huang, Z. Liu, J. Miao, N. Li, W. Su, $(Ba_{0.5}Sr_{0.5})(Fe_{0.8}Zn_{0.2})O_{3-\delta}$ perovskite oxide as a novel cathode for intermediate-temperature solid-oxide fuel cells, J. Am. Ceram. Soc. 90 (2007) 2264–3366.
[26] B. Wei, Z. Lü, X. Huang, M. Liu, J. Miao, N. Li, W. Su, Synthesis, electrical and electrochemical properties of $(Ba_{0.5}Sr_{0.5})(Fe_{0.8}Zn_{0.2})O_{3-\delta}$ perovskite oxide for IT-SOFC cathode, J. Power Sources 176 (2008) 1–8.
[27] A. Feldhoff, M. Arnold, J. Martynczuk, T. Gesing, H. Wang, The sol–gel synthesis of perovskites by an EDTA/complexing method involves nanoscale solid state reactions, Solid State Sci. 10 (2008) 689–701.
[28] J. Martynczuk, K. Efimov, L. Robben, A. Feldhoff, Performance of zinc-doped perovskite-type membranes at intermediate temperatures for long-term oxygen permeation and under a carbon dioxide atmosphere, J. Membr. Sci., 2009, in press, doi:10.1016/j.memsci.2009.07.035.
[29] A. Feldhoff, J. Martynczuk, H. Wang, Advanced $(Ba_{0.5}Sr_{0.5})(Fe_{0.8}Zn_{0.2})O_{3-\delta}$ perovskite-type ceramics as oxygen selective membranes: evaluation of the synthetic process, Prog. Solid. State. Chem. 35 (2007) 339–353.
[30] J. Martynczuk, M. Arnold, H. Wang, A. Feldhoff, How $(Ba_{0.5}Sr_{0.5})(Fe_{0.8}Zn_{0.2})O_{3-\delta}$ and $(Ba_{0.5}Sr_{0.5})(Co_{0.8}Fe_{0.2})O_{3-\delta}$ perovskites form via an EDTA/citric acid complexing method, Adv. Mater. 19 (2007) 2134–2140.
[31] M. Arnold, H. Wang, J. Martynczuk, A. Feldhoff, In situ study of the reaction sequence in the sol–gel synthesis of a $(Ba_{0.5}Sr_{0.5})(Co_{0.8}Fe_{0.2})O_{3-\delta}$ perovskite by X-ray diffraction and transmission electron microscopy, J. Am. Ceram. Soc. 90 (2007) 3651–3655.
[32] H. Schmid, W. Mader, Oxidation states of Mn and Fe in various compound oxide systems, Micron 37 (2006) 426–432.
[33] P. Adler, S. Ericsson, Structural properties Mössbauer spectra and magnetism of perovskite-type oxides $SrFe_{1-x}Ti_xO_{3-y}$, Z. Anorg. Allg. Chem. 626 (2000) 118–124.
[34] A. Bocquet, A. Fujimoro, T. Mizokawa, T. Saitoh, H. Namatame, S. Suga, N. Kimizuka, Y. Takeda, M. Takano, Electronic structure of $SrFe^{4+}O_3$ and related Fe perovskite oxides, Phys. Rev. B 45 (1992) 1561–1570.
[35] P. Potapov, N. Schryvers, Measuring the absolute position of EELS ionisation edges in a TEM, Ultramicroscopy 99 (2004) 73–85.
[36] K. Lagarec, D.G. Rancourt, Recoil—Mössbauer Spectral Analysis Software for Windows, version 1.02, Department of Physics, University of Ottawa, Ottawa, 1998.
[37] W. Gruner, Determination of oxygen in oxides by carrier hot gas extraction analysis with simultaneous CO_x detection, Fresenius J. Anal. Chem. 365 (1999) 597–603.
[38] H. Küppers, Thermal expansion, in: A. Authier (Ed.), International tables for crystallography, International Union of Crystallography, vol. D, Kluwer Academic Publishers, Dordrecht, 2003, pp. 99–104.

[39] H. Wang, T. Schiestel, C. Tablet, M. Schroeder, J. Caro, Mixed oxygen ion and electron conducting hollow fiber membranes for oxygen separation, Solid State Ionics 177 (2006) 2255–2259.
[40] M. Arnold, J. Martynczuk, K. Efimov, H. Wang, A. Feldhoff, Grain boundaries as barrier for oxygen transport in perovskite-type membranes, J. Membr. Sci. 316 (2008) 137–144.
[41] J. Martynczuk, M. Arnold, A. Feldhoff, Influence of grain size on the oxygen permeation performance of perovskite-type $(Ba_{0.5}Sr_{0.5})(Fe_{0.8}Zn_{0.2})O_{3-\delta}$ membranes, J. Membr. Sci. 322 (2008) 375–382.
[42] F. de Groot, X-ray absorption and dichroism of transition metals and their compounds, J. Electr. Spectrosc. Rel. Phenom. 67 (1994) 529–622.
[43] C. Dong, C. Persson, L. Vayssieres, A. Augustsson, T. Schmitt, M. Mattesini, R. Ahuja, C. Chang, J. Guo, Electronic structure of nanostructured ZnO from X-ray absorption and emission spectroscopy and the local density approximation, Phys. Rev. B 70 (2004) 1953 251–1953 252.
[44] J.B. Goodenough, J.M. Longo, Crystallographic and magnetic properties of perovskite and perovskite-related compounds, in: K.H. Hellwege, A.M. Hellwege (Eds.), Landolt–Börnstein New Series Numerical Data and Functional Relationships in Science and Technology, vol. III/4a, Springer, Berlin, 1970, pp. 126–314.
[45] F. de Groot, M. Grioni, J. Fuggle, J. Ghijsen, G. Sawatzky, H. Petersen, Oxygen 1s X-ray-absorption edges of transition-metal oxides, Phys. Rev. B 40 (1989) 5715–5723.
[46] The RT Fe$-L_{2,3}$ spectra of standard substances are accessible as ascii data through the EELS data base at the Centre d'Elaboration de Matériaux et d'Etudes Structurales (CEMES): 〈http://www.cemes.fr/eelsdb/〉.
[47] H. Ikeno, I. Tanaka, T. Miyamae, T. Mishimna, H. Adachi, K. Ogasawara, First principles calculation of Fe $L_{2,3}$-edge X-ray absorption near edge structures of iron oxides, Mater. Trans. 45 (2004) 1414–1418.
[48] I. Tanaka, T. Mizoguchi, T. Yamamoto, XANES and ELNES in ceramic science, J. Am. Ceram. Soc. 88 (2005) 2013–2029.
[49] L. Garvie, P. Buseck, Ratios of ferrous to ferric iron from nanometre-sized areas in minerals, Nature 396 (1998) 667–670.
[50] K. Krishnan, Iron $L_{2,3}$ near-edge fine structure studies, Ultramicroscopy 32 (1990) 309–311.
[51] P. van Aken, B. Liebscher, V. Styrsa, Quantitative determination of iron in oxidation states in minerals using Fe $L_{2,3}$ electron energy-loss near-edge structure spectroscopy, Phys. Chem. Miner. 25 (1998) 323–327.
[52] A. Gloter, J. Ingrin, D. Bouchet, C. Colliex, Composition and orientation dependence of the O K and Fe $L_{2,3}$ fine structures in $Ca_2(Al_xFe_{1-x})_2O_5$, Phys. Rev. B 61 (2000) 2587–2594.
[53] A. Sefat, G. Amow, M. Wu, G. Botton, J. Greedan, High-resolution EELS study of the vacancy-doped metal/insulator system $Nd_{1-x}TiO_3$, $x = 0$ to 0.33, J. Solid State Chem. 178 (2005) 1008–1016.
[54] T. Wagener, Y. Gao, J. Weaver, A. Arko, B. Flandermeyer, D. Capone, Unoccupied electronic states and surface phenomena for $YBa_2Cu_3O_{6.9}$, Phys. Rev. B 36 (1987) 3899–3902.
[55] M. Abbate, F. de Groot, J. Fuggle, A. Fujimori, O. Strebel, F. Lopez, M. Domke, G. Kaindl, G. Sawatzky, M. Takano, Y. Takeda, H. Eisaki, S. Uchida, Controlled-valence properties of $La_{1-x}Sr_xFeO_3$ and $La_{1-x}Sr_xMnO_3$ studied by soft-X-ray absorption spectroscopy, Phys. Rev. B 46 (1992) 4511–4519.
[56] N. Greenwood, T. Gibb, Mössbauer Spectroscopy, Chapman & Hall, London, 1971.
[57] F. Menil, Systematic trends of the ^{57}Fe Mössbauer isomer shifts in (FeO_n) and (FeF_n) polyhedra. Evidence of a new correlation between the isomer shift and the inductive effect of the competing bond T–X ($\rightarrow$Fe) where X is O or F and T any element with a formal positive charge, J. Phys. Chem. Solids 46 (1985) 763–789.
[58] R. Parish, NMR, NQR, EPR, and Mössbauer Spectroscopy in Inorganic Chemistry, Ellis Horwood, New York, Berlin, 1990.
[59] V. Bhide, H. Bhasin, Mössbauer study of the $SrTiO_3$:Co^{57} system, Phys. Rev. 159 (1967) 586–593.
[60] B. Shankar, H. Steinfink, Synthesis structure and properties of $LaSr_3Fe_{3-x}Ga_xO_{10-\delta}$: Fe^{3+} an intermediate spin state, J. Solid State Chem. 122 (1996) 390–393.
[61] W. Xu, O. Naaman, G. Rozenberg, M. Pasternak, R. Taylor, Pressure-induced breakdown of a correlated system: the progressive collapse of the Mott–Hubbard state in $RFeO_3$, Phys. Rev. B 64 (2001) 944111–944119.
[62] A. Maradudin, P. Flinn, S. Ruby, Velocity shift of the Mössbauer resonance, Phys. Rev. 126 (1962) 9–23.
[63] V. Šepelák, S. Wißmann, K. Becker, A temperature-dependent Mössbauer study of mechanically activated and non-activated zinc ferrite, J. Mater. Sci. 33 (1998) 2845–2850.
[64] S. Adler, Chemical expansivity of electrochemical ceramics, J. Am. Ceram. Soc. 84 (2001) 2117–2119.
[65] A. Fossdal, M. Menon, I. Waernhus, K. Wiik, M. Einarsrud, T. Grande, Crystal structure and thermal expansion of $La_{1-x}Sr_xFeO_{3-\delta}$ materials, J. Am. Ceram. Soc. 87 (2004) 1952–1958.
[66] K. Asai, O. Yokokura, N. Nishimori, H. Chou, J. Tranquada, G. Shirane, S. Higuchi, Y. Okajima, K. Kohn, Neutron scattering study of the spin-state transition and magnetic correlations in $La_{1-x}Sr_xCoO_3$ ($x = 0$ and 0.08), Phys. Rev. B 50 (1994) 3025–3032.
[67] G. Hearne, M. Pasternak, R. Taylor, P. Lacorre, Electronic structure and magnetic properties of $LaFeO_3$ at high pressure, Phys. Rev. B 51 (1995) 11495–11500.
[68] R. Shannon, Revised effective ionic radii and systematic studies of interatomic distances in halides and chalgogenides, Acta Crystallogr. A 32 (1976) 751–767.
[69] M. Valkeapää, Y. Katsumata, I. Asako, T. Motohashi, T. Chan, R. Liu, J. Chen, H. Yamauchi, M. Karppinen, Charge compensation and oxidation in $Na_xCoO_{2-\delta}$ and $Li_xCoO_{2-\delta}$ studied by XANES, J. Solid State Chem. 180 (2007) 1608–1615.
[70] P. Raccah, J. Goodenough, First-order localized-electron $\rightleftharpoons$ collective-electron transition in $LaCoO_3$, Phys. Rev. 155 (1967) 932–943.
[71] V. Bhide, D. Rajoria, G.R. Rao, C. Rao, Mössbauer studies of the high-spin-low-spin equilibria and the localized-collective electron transition in $LaCoO_3$, Phys. Rev. B 6 (1972) 1021–1032.
[72] K. Kamata, T. Nakamura, T. Sata, State of d-electrons in perovskite-type compounds ABO_3, Bull. Tokyo Inst. Technol. 120 (1974) 73–79.
[73] R. Roy, Rational molecular engineering of ceramic materials, J. Am. Ceram. Soc. 60 (1977) 350–363.
[74] L. Gauckler, D. Beckel, B. Buergler, E. Jud, U. Muecke, M. Prestat, J. Rupp, J. Richter, Solid oxide fuel cells: systems and materials, Chimia 58 (2004) 837–850.